A non-invasive study of flow dynamics in membrane distillation hollow fiber modules using low-field nuclear magnetic resonance imaging (MRI)

X Yang[1,2], E.O Fridjonsson[3], M L. Johns[3], R Wang*[,1,2], A G. Fane[1,2]

1. Singapore Membrane Technology Centre, Nanyang Technological University, Singapore 639798
2. School of Civil and Environmental Engineering, Nanyang Technological University, Singapore 639798
3. School of Mechanical and Chemical Engineering, University of Western Australia, Western Australia 6009

*Corresponding author at: School of Civil and Environmental Engineering,

Nanyang Technological University, 639798 Singapore,

Singapore. Tel.: +65 6790 5327; fax: +65 6791 0676.

E-mail address: rwang@ntu.edu.sg (R. Wang).

Abstract

Low-field bench-top nuclear magnetic resonance imaging (MRI) has been applied to investigate the hydrodynamics in novel hollow fiber modules designed for the membrane distillation (MD) process. Imaging, spatially resolved velocity maps and propagators (probability distributions of displacement/velocity) were all acquired in the modules with flow in the shell side. This was performed for four fiber configurations randomly-packed fibers, spacer-knitted fibers, curly and semi-curly fiber, and correlated with overall module performance. This revealed significantly more transverse flow for the curly configuration, and hence enhanced mixing, compared to the randomly packed configuration; this was consistent with an enhanced membrane performance (permeation flux). Conversely the spacer knitted fiber configuration revealed significant flow channeling in the centre of the module, despite presenting enhanced membrane performance. However propagator data for this configuration revealed reduced stagnant regions and significant transverse flow, which we speculate indicates better overall module mixing that suggested by the acquired localized velocity image.

1. Introduction

As an alternative for seawater desalination, membrane distillation (MD) is a promising technique credited with several advantages: low sensitivity to salt concentration and theoretically 100% salt rejection; feasibility to utilize low-grade heat and renewable energy (*e.g.*, waste heat or solar power); low vulnerability to membrane fouling and good performance under mild operating conditions as compared to conventional, multi-stage distillation or reverse osmosis (RO)[1].Despite many attractive characteristics and extensive lab-scale studies, MD has not been widely implemented in industry[1, 2].One of the major challenges impeding its application is flow mal-distribution and/or poor mixing and hence severe local temperature polarization (TP) that compromises module performance[3].

As a preferable configuration for industrial applications, hollow fiber modules present more versatility, larger membrane area per unit volume, reduced vulnerability to TP[4] and enhanced productivity. Nevertheless, many prior studies on general hollow fiber module work have shown that non-ideal flow distribution in a module will lead to less active membrane area, insufficient mixing and local loss of driving force, and hence low heat-or mass-transfer efficiencies[5-12].Studies on hydrodynamic improvement in MD hollow fiber modules are sparse in the open literature, mainly due to fabrication and modeling complications[2, 13-16].Enhancing strategies such as flow alteration aids or modifying fiber geometries to create secondary flows or eddies (such as novel fiber configurations or turbulence promoters, *e.g.* spacers or baffles) have been proposed for improving MD module performance [15-17]. In the MD process employing shell-side feed, the occurrence of significant channeling, bypassing, or dead zones can greatly reduce the local driving

force and decrease module performance. Particularly, our previous work on hollow fiber module design showed that the fluid flow across the fiber bundles needs to be evenly distributed in order to achieve an effective mitigation of TP and improvement of the MD process efficiency. For a direct understanding of the fluid dynamics fundamentals, physical inspection of the module inner structures/fiber arrangement and flow distribution is essential in providing valuable insights for future optimum module design work.

Traditionally, there are many approaches for characterizing flow distribution: broadly these are invasive or non-invasive. Invasive or quasi-invasive techniques include structural inspection by disassembling the module parts [18], tracer analysis[19], combined X-ray computed tomography (CT) scanner and radio-opaque tracer dye study and/or high-speed tracer photography[20-22]. However, to achieve in-situ real-time monitoring of the flow field inside a confined opaque vessel, non-invasive techniques are preferred, such as optical examination and non-optical methods. However, optical methods are only restricted to special conditions such as transparent membranes [23]or fluorescent tracers. As a non-optical technique, nuclear magnetic resonance (NMR) has various advantages including being non-invasive, the absence of ionizing radiations, freedom to image any selected plane through a complex sample (or generate a 3-dimensional image of the sample as a whole) and the ability to image non-metallic samples which are optically opaque[24], which is an ideal feature for the MD modules composed of opaque plastics..

. NMR involves the excitation and relaxation of various nuclei under the influence of a magnetic field. In this work we exclusively consider ^{1}H signal [25],which originates predominately from the water content of our modules. The signal strength is proportional

to ^{1}H density modulated by various signal relaxation processes. The application of magnetic field gradients allows both imaging and displacement (self-diffusion and velocity). These can be combined to deliver velocity maps, in which velocity is measured for each pixel in the image; alternatively probability distributions of displacement (converted to velocity) can be measured, these are known as propagators [24-26].

Early module studies used NMR flow imaging to elucidate flow distribution in inorganic tubular configurations by mapping the axial flow velocities and verifying with theoretical modeling results [27, 28]. Membrane bioreactor researchers also explored the capability of NMR imaging technique for observing starling flows in the shell side of hollow fiber modules [29, 30].Studies using both structural and velocity imaging has occurred in both hollow fiber membrane modules [31] and spiral would membrane modules [32, 33]. Applications of MRI to hemodialyzer modules containing thousands of fibers revealed significant flow mal-distribution despite the presence of turbulence promoters [34-36].

Despite its clear advantages and ability to inform module development, the use of MRI in such a capacity is limited. This is undoubtedly due to geometric constraints on the modules as well as comparatively poor signal to All above-mentioned studies have adopted super-conductive or high-field NMR techniques with a ^{1}H resonance frequencies up to 600 MHz. This is understandable given the greater signal-to-noise available; SNR $\propto (B_0)^{7/4}$, where B_0 is the magnetic field strength. However these systems are expensive, consequently limited in availability, immobile and generally require expert operators.

Consequently in the current study we employ a bench-top NMR spectrometer featuring a 0.3 T permanent magnet and a ^{1}H resonance frequency of 12.7 MHz. This presents comparatively simpler operation, easier maintenance, greater mobility and significantly lower cost and footprint, meaning it should in principle be accessible to a broader range of scientists and engineers. Using this apparatus we measure the flow-field in four MD hollow fiber module designs (conventional randomly-packed, spacer-knitted, semi-curly and curly fiber modules). 2D structural and velocity images as well as velocity propagators are acquired and correlated against membrane performance. We also consider the compromise involved in applying this bench-top apparatus compared to a high-field super-conducting system.

.

2. Experimental protocol

2.1 Hollow fiber module preparation and MD performance tests

In this current study Polyvinylidene fluoride (PVDF) hollow fiber membranes, of which MD related properties were characterized in our previous work [5, 37], were used to fabricate lab-scale multi-fiber MD modules. The fibers were potted into the housings that are made by transparent Acrylic material to facilitate direct surface observation of the fiber bundles, as shown in Fig. 1. Four different module configurations (Fig. 1) were assembled in various ways (*i.e.*, modules with randomly-packed, spacer-knitted, curly and semi-curly fibers) with specifications as given in Table 1: inner diameter 19 mm and effective length 450 mm; packing density of 30%; and membrane area of 0.1−0.11 m^2. In this study a

randomly packed module, which contained 51 randomly packed fibers, was fabricated and used as the conventional module benchmark. Besides the semi-curly fiber configuration, which is considered as a compromised design to reduce the fabrication complexity, the assembly procedures for modules of different patterns can be found in our previous work [17]. In the module fabrication process, care must be taken to avoid damaging the membrane surface.

The experimental setup used to evaluate the MD performance tests for all hollow fiber modules is shown in our previous work [37]. Both the feed and permeate solutions were cycled through the hollow fiber module in countercurrent mode. For the performance tests using synthetic seawater (3.5 wt% sodium chloride solution), the operating details can also be found in the literature[37].

2.2 NMR experimental protocol

The NMR experiments were conducted using an Oxford MARAN low-field bench-top MRI system employing a 0.3 Tesla permanent magnet with a (^{1}H) resonance frequency of 12.7 MHz. The system features a sample access of 53 mm in diameter, any practical length and accommodates 3D magnetic field gradients for spatial encoding. The experimental setup for flowing experiments through the shell side of the multi-fiber membrane modules is shown in Fig. 2.

In this experiment each membrane module was installed and tested individually in the

5.3-cm i.d. resonator RF probe. De-ionized water (DI) was used as the flowing fluid and circulated through the shell side using a peristaltic pump, which was calibrated using NMR velocity imaging of water in an equivalent pipe. The imaging planes were chosen as both parallel- and perpendicular-to-flow directions (*i.e.*, module's axial Y and transverse Z directions, respectively), allowing the cross section and side view of a module to be analyzed. Conventional MRI pulse sequences were used to acquire images, velocity images/maps and propagators. 2D Images were acquired over afield of view of 30 mm x 30 mm employing 128 pixels in each dimension (in-plane resolution of 234 mm) and a slice thickness of 5 cm. In terms of velocity encoding, magnetic field gradient strength was varied in 128 increments for propagator acquisition (g_{max} = 64 mT/m, δ = 4 ms, Δ = 100 ms) whilst the strength employed for velocity imaging was varied depending on the velocity to avoid signal phase fold-over (δ = 4 ms, Δ = 20 ms). Total acquisition times of propagators, 2D images and 2D velocity maps were 34, 34, and 68 minutes, respectively.

2.3 Flow calibration and error assessment

All the above-mentioned experiments were repeated and showed reproducible results. The flow rate of the pump was calibrated using NMR velocity imaging and volumetric throughput measurements of water, which showed excellent agreement (error within ±5%). In the MD performance experiments, the results for the water-flux fluctuations were also within ±5% (illustrated as error bars in the figures). The temperature and flow rate variations were strictly controlled within ±0.2°C and ± 10mL/min.

3. Theoretical basis for NMR signal analysis

NMR signal is caused by the interaction of the nuclear spin (or quantized angular momentum) of a nuclei (*e.g.*, ^{1}H) with an external magnetic field (B_0), causing spin resonance at the Larmor frequency (ω_0). The basic principle of MRI (and displacement measurements) is to spatially encode the spins by superposition of constant magnetic field gradient G onto a static magnetic field [23]. The change in phase (φ) of the NMR signal is proportional to the spin displacement ($\mathbf{r}'(t)$),

$$\frac{d\varphi}{dt} = \gamma G \mathbf{r}'(t) \tag{1}$$

Where G is the linear magnetic field gradient applied across the sample, γ is the gyromagnetic ratio of the nuclei (*e.g.* ^{1}H).

Pulsed Field Gradient (PFG) NMR [35] can be used to measure the probability distribution of displacement (*i.e.* propagator). The characteristic diffusion coefficient and mean displacement have a close relation with the propagator, which is defined as the probability density of a diffusing molecule (*e.g.*, starting at t=0 and location r and propagating to $r+R$ after time $t=\Delta$). As an inverse Fourier transform of the acquired PFG NMR signal, the averaged propagator $\bar{P}$ is given as:

$$\bar{P}(R,\Delta) = \int_{V} P(r|r+R,\Delta) p_0(r) \, dr \tag{2}$$

where $p_0(r)$ is the initial signal probability distribution as a function of initial position r.

When analyzing the probability distributions of displacement a useful analysis framework is the central moment:

$$\mu_n = \left\langle \left(x - \mu\right)^n \right\rangle = \int_{-\infty}^{\infty} \left(x - \mu\right)^n P(x) \, dx \tag{3}$$

Where μ_n is the nth central moment, μ is the first raw moment (*i.e.* mean), P(x) is the normalized probability distribution as function of displacement (x). The second central moment (*i.e.* variance) is used to quantify the uniformity of flow, and the spread of the residence time distribution (RTD). Its magnitude generally scales with increasing heterogeneity as wider distributions (*e.g.* long break-through tails) will increase its value.

4. Results and discussion

4.1 Water molecule contrast NMR imaging

To acquire a direct display of the fiber arrangements, 2D images of the different designs (*i.e.*, randomly packed, spacer-knitted, semicurly- and curly-fiber modules) filled with stationary DI water were acquired transverse and parallel to the module axis. These are presented in Fig. 3. The thickness of the excited slice is 5 cm. With the signal originating from the water content on the shell side of the module, the fiber matrix is revealed. Well defined fibers in the transverse plane are aligned perpendicular to the slice direction; as expected these are least prominent in the curly-fiber module (Fig. 3d) and most prominent in the randomly packed module (Fig. 3a). In the axial direction, the semi-undulating flow paths between the curly-fiber modules are revealed.

4.2 PFG NMR diffusion/ propagator experiments

To evaluate the mixing intensity and fluid dynamics induced by different designed channels, water propagators were measured parallel (Y) and perpendicular (Z) to the superficial flow direction with flowing fluid (DI water) at 100 mL/min for an observation time of 100 ms. These are presented in Fig. 4. In general the Y-direction propagators present an asymmetric distribution with a greatest probability of finding water molecules around zero velocity, indicative of fluid holdup. It is evident that the spacer knitted design shows reduced holdup and comparatively better hydrodynamics; the three other designs present similar hydrodynamics.

In the transverse Z direction (Fig. 4b), the greatest probability is for zero velocity, consistent with minimal transverse flow and significant stagnant zones as evidenced in Fig 4a. The greatest transverse flow is observed for the curly design, consistent with the undulating designs intention of promoting mixing. Broadly the propagator measurements serve to be a useful insight into the internal hydrodynamics and hence mixing in the modules.

4.3 NMR velocity mapping

The velocity maps in a transverse slice (for velocity in the superficial flow direction) are shown in Fig. 5 for the four module designs over a slice thickness of 5 cm at a flow rate of 100mL/min over an observation time of 100 ms. What is immediately obvious is the loss

of signal from the centre of the spacer-knitted design – this will be discussed further below. All other three designs present mean velocities consistent with gravimetric measurements. It appears that a more homogeneous flow-field is evident for the semi-curly fiber design followed by the curly fiber design and finally the randomly packed design. The standard deviation (σ) obtained for the NMR velocity maps are spacer-knitted $\sigma = 1.6$ mm/sec, semi-curly $\sigma = 3.9$ mm/sec, curly $\sigma = 7.7$ mm/sec and random $\sigma = 8.2$ mm/sec.

Fig. 6 shows a comparison of module efficiency for four designs via MD temperature experiments at feed and permeate flow rates of 3 L/min and 0.4 L/min, respectively.. Undoubtedly, the permeation fluxes of all MD modules follow a classical exponential increase with increasing feed temperature [39]. Compared to the randomly packed module, significant flux enhancement is achieved using modified configurations. The highest flux improvement of up to 92 % was observed by the modules with extensive undulating membrane surface (curly fibers and spacer-knitted) at a feed temperature of 343 K.

The loss of signal in the spacer-knitted design is indicative of comparatively high displacements in this central channel and consequential loss of signal due to shear-induced T_2 signal relaxation. We proceed to explore this phenomenon more thoroughly in the next section

4.4 NMR Flow analysis for spacer-knitted module

4.4.1   Imaging vs. flow rate for spacer-knitted module

To further elucidate the hydrodynamics of the shell side of the spacer-knitted module, the relationship between the NMR signal detection and operating flow conditions were investigated. Fig. 7 presents a series of cross-sectional images for the spacer-knitted configuration by applying a gradual increase on the shell-side volumetric flow rates from 10 to 2500 mL/min (i.e., 0.017 to 41.7mL/s), with a selected slice thickness of 5 cm and an echo time of 29.5ms (This is a long echo time given the large dispersions due to high flow rates, small pixel size (240x240μm) and low signal-to-noise ratio (~10)). Similar to what has been observed in Fig. 5b, a "black hole" (signal loss) starts to appear in the center of the module when the flow rate increases to 40 mL/min, and drastically enlarges with further increasing flow velocity till a complete loss of signal at 2500 mL/min. This phenomenon is consistent with localized channeled flow with increasing externally-applied flow rates.

Again, although the pixel information obtained from velocity maps is not sufficient for quantifying the flow status, a qualitative comparison on the signal loss caused by regional fast flow (large displacement) is rather useful in analyzing the flow transition for such special case as the spacer-knitted module. Hence, a plot of NMR signal magnitude as a function of volumetric flow rate at the shell side of the spacer-knitted module is given in Fig. 8, in which an initial significant decrease on the slope at a lower flow rate range and then a gradual decline occur. This finding supports our previous statement that this configuration allows the transition of a sudden occurrence of fast regional flow (with correspondence to the results in Fig. 7) and a subsequent tendency for an even flow distribution to slowly take place through the entire channel.

4.4.2 *Probability distribution vs. flow rate for spacer-knitted module-don't warrant their own section – combine with above.*

To quantitatively confirm the statements made from Figs. 7 & 8, propagator experiments were conducted with flowing DI water at the shell-side ofthe spacer-knitted module in both parallel- (Y) and perpendicular-to-flow (Z) directions, at an increasing volumetric flow rate from 20 to 400 mL/min. Fig. 9 gives the normalized displacement distribution in terms of flow velocity at different flow conditions. It is observed that with increasing flow rate the height of the distribution curve decreases significantly while the width (dispersion) increases at the axial Y direction, as shown in Fig. 9a; Similar to what was observed from the propagators in Fig. 4a, this is because that at a lower flow rate there is a higher probability of finding water molecules at small displacement (0 mm). Hence, the distribution curve tends to have a relative symmetric shape under such applied flow condition (*e.g.*, at 20 mL/min). As the flow rate increases, the probability curve is more spread out and becomes more asymmetric, *i.e.*, a longer tail at the large displacement side (*e.g.*, at 400 mL/min).Therefore, it gives a lower probability at small displacement and more molecules found at larger displacements relative to a low flow rate condition. This is an indication of more intensive flow interaction taken place induced by the combination of faster externally-applied flow condition and internally-altered flow channel. In the transverse Z direction (Fig. 9b), the probability distribution curve lowers and widens as the applied volumetric flow rate increases. This is very encouraging information for expecting a strong transversal mixing and a subsequent improvement on the overall flow distribution.

However, due to the limitations of NMR signal detection, a further increase on the flow rate seem to greatly increase the difficulty in tracking fast moving molecules from such a thin selected slice and interpreting the signal. Without considering the absolute pixel counts of propagators shown in Fig. 8, an analysis of the normalized probability distribution at two extremely different flow rates is given in Fig. 10– 400 mL/min with an acceptable level of signal loss (approximately 57% signal detected based on Fig. 8) and1500 mL/min (only less than 10% signal detected based on Fig. 8). In contrast to the trend observed in Fig. 9, both Y and Z direction propagators at 1500 mL/min are relatively narrower and has a much higher probability finding water molecules at small displacement (0 mm), compared to that of 400 mL/min. One reason is that a significant signal loss occurred in large displacement regimes, which corresponds favorably with the pixel comparison provided in Fig. 8. The other possible cause is due to the formation of vortices and subsequent circulation of certain molecules results in signal offset at a high flow rate of 1500 mL/min.

4.4.3 Variance vs. flow rate for spacer-knitted module

As an important parameter in conventional flow analysis in a confined vessel, the variance (or standard deviation)shows the degree of dispersion around the mean displacement, *i.e.*, the spread of the flow distribution curve. A large value indicates a big deviation from a uniform flow pattern. An ideal flow would have a small variance with a high mean, indicative of a homogenous mixing with molecules at large displacement regimes. Therefore, a variation of the variance can provide valuable information in

revealing the relationship between the probability distribution function (pdf) and flow behaviors. Thus, to understand the flow dispersion mechanism in a channel as the applied flow conditions change, a calculation on the second central moment — variance (Eq. (3), n=2) based on the propagators was conducted. Fig. 10 presents the variance as a function of the volumetric flow rate at the shell-side of the spacer-knitted module, in both parallel-to-flow Y and transversal Z directions. It is noted that in both flow directions the variance is first increases and then drastically decreases with increasing flow rate. Clearly, this has violated the conventional trend of variance in a developing flow – an initial and a subsequent plateau value under complete mixing is reached. This violation, however, can be explained by the corresponding NMR signal loss detected in the propagators (Fig. 9) due to the high speed inflow and outflow. The changes on the variance may also identify a shift on the dispersion mechanism (*i.e.*, mechanical, Taylor or hold-up dispersion), which is not discussed in this paper.

4.5 Overall comparison for all modules

For a thorough evaluation of the flow behaviors in all four modules, key moments such as the mean displacement (mm, Eq (3), n=1), variance (mm^2, Eq. (3), n=2) and skewness (mm^3, Eq. (4), n=3) are calculated and compared based on the propagator experiments, as shown in Table 2. At an observation time of 100 ms, in the parallel-to-flow Y direction both the curly and semi-curly modules show relatively higher mean displacement; while the spacer-knitted one presents the lowest value, relative to the benchmark (randomly-packed

module). Consistent with the module performance as well as NMR velocity images, the curly-fiber design presents the lowest deviation and a high mean — implying the existence of an even flow distribution with fast flowing fluid. Similarly, in the transversal Z direction the curly fiber module shows more vigorous molecular movement and homogeneous mixing, with a larger mean displacement as well as a high variance; on the contrary, the randomly-packed module shows the lowest mean (negative) and variance in this direction, possibly caused by the existence of liquid stagnation or slight back flow.

Overall, this moment analysis corresponds well with the MD performance shown in Fig. 6 and our previous MD studies [17], which indicated that the heat-transfer process could be enhanced by modifying the flow channel and/or increasing the velocity and to reduce the thermal boundary layer on the membrane surface *.i.e.*, when the temperature at the membrane surface approaches the temperature in the bulk permeate, the driving force for vapor transport through the membrane can be maximized. In general, the modules with undulating membrane surface (e.g., curly and spacer-knitted fibers) show advantages by achieving higher vapor permeability and mitigating TP effect with reasonably lower energy losses; this is mainly due to the enhanced shell-side hydrodynamics induced by altered fiber geometries and relatively uniform shell-side flow distribution, which are confirmed by this current NMR study.

5. Conclusions

With the aid of nuclear magnetic resonance imaging (MRI) technique, the hydrodynamic conditions and flow distribution in membrane distillation (MD) hollow fiber modules were studied. The pulse field gradient (PFG) experimental technique was used to acquire the molecular displacement information in the various flow channels. As an evaluation of module efficiency, the molecular contrast cross-section imaging, diffusion and propagator experiments in the shell-side flow, and the velocity mapping for all studied design patterns were conducted.

The results showed that compared to the conventional randomly-packed module, the curly fiber design presented a narrower water propagator at Z (perpendicular-to-flow) direction, a higher probability of water molecules at high displacement at Y (parallel-to-flow) direction, and more intense local mixing and improved hydrodynamics revealed through its velocity map, which agreed well with the MD performance assessment. However, as a well-performed configuration testified via membrane process experiments, the spacer-knitted module showed a surprisingly significant NMR signal loss at high displacement, which indicated a poor hydrodynamics. Fortunately, this quest was unveiled via further propagator experiments at a much higher volumetric flow rate. Meanwhile, this issue has suggested the potential limitations on spatial resolution using the NMR instruments to assess hydrodynamics in a complex flow channel.

In summary, this study has demonstrated the capability of a low-field NMR instrument to analyze the fluid dynamics non-invasively could therefore greatly assist in implementing

novel module design and determining the optimum operating conditions in membrane separation.

Acknowledgments

Nomenclature

A	Effective membrane area, m^2
C	Mass-transfer coefficient or membrane-distillation coefficient, $kg \cdot m^{-2} \cdot h^{-1} \cdot kPa^{-1}$
$C(t)$	Temporal tracer concentration at the effluent, $mol \cdot m^{-3}$
c_0	Pulse injection tracer concentration at the feed entrance, $mol \cdot m^{-3}$
d_o	Outer diameter of the hollow fiber, mm
d_s	Housing diameter of the module, mm
E_t	Tensile modulus, MPa
H	Effective heat-transfer coefficient based on the temperature difference across the entire membrane, $W \cdot m^{-2} \cdot K^{-1}$
h	Overall heat-transfer coefficient $\equiv \dfrac{1}{h_f} + \dfrac{1}{h_p}$, $W \cdot m^{-2} \cdot K^{-1}$
h_f	Feed-side local heat-transfer coefficient, $W \cdot m^{-2} \cdot K^{-1}$
h_p	Permeate-side local heat-transfer coefficient, $W \cdot m^{-2} \cdot K^{-1}$
k_m	Thermal conductivity of membrane, $W \cdot m^{-1} \cdot K^{-1}$
L	Effective fiber length, mm
M	Molecular weight of water, $g \cdot mol^{-1}$
m	Total amount of tracer, mol
n	Number f fibers
N	Vapor flux, $kg \cdot m^{-2} \cdot h^{-1}$

P	Vapor pressure of the bulk streams, kPa
q	Total heat flux, $W \cdot m^{-2}$
q_c	Conductive heat loss through the membrane, $W \cdot m^{-2}$
q_v	Latent heat flux, $W \cdot m^{-2}$
Q_f	Feed flowrate, $L\ min^{-1}$
Q_p	Permeate flow rate, $L\ min^{-1}$
Q_0	Influent flow rate in tracer study, $m^3 \cdot s^{-1}$
R	Gas constant, $8.314\ J \cdot K^{-1}$
Re	Reynolds number, $\dfrac{d_h \nu \rho}{\mu}$
r_{max}	Maximum pore size, μm
r_{mean}	Mean pore size, μm
T_f	Bulk temperature of the feed, K
T_{fm}	Temperature at the membrane surface on the feed side, K
T_m	Membrane temperature, K
T_p	Bulk temperature of the permeate, K
T_{pm}	Temperature at the membrane surface on the permeateside, K
ΔT	Bulk temperature difference, K
t	Time, s
t_m	Mean residence time, s
$\bar{t}$	Theoretical residence time of the vessel V/Q_0, s
V	Volume of the vessel, m^3

v_f	Recirculated feed velocity, m·s^{-1}
v_p	Recirculated permeate velocity, m·s^{-1}

Greek letters

ε	Membrane porosity, %
ϕ	Module packing density, %
τ	Temperature-polarization coefficient (TPC)
σ^2	Variance, s^2
$\sigma_\theta^{\ 2}$	Dimensionless variance
θ	Dimensionless time
δ_b	Strain at fiber breakage,%
δ_m	Membrane thickness, μm
γ	latent heat-of-vaporization, J·kg^{-1}
ρ	Density of water, kg·m^{-3}
μ	Viscosity of water, Pa·s

Subscripts

f	Feed
p	Permeate

References

[1] K. W. Lawson and D. R. Lloyd, Membrane distillation, Journal of Membrane Science, 124 (1) (1997) 1-25

[2] M. S. El-Bourawi, Z. Ding, R. Ma and M. Khayet, A framework for better understanding membrane distillation separation process, Journal of Membrane Science, 285 (1-2) (2006) 4-29

[3] R. W. Schofield, A. G. Fane and C. J. D. Fell, The efficient use of energy in membrane distillation, Desalination, 64 (1987) 231-243

[4] R.W. Schofield, A.G. Fane and C. J. Fell, Heat and mass transfer in membrane distillation, Journal of Membrane Science, (33) (1987) 299-313

[5] X. Yang, R. Wang and A. G. Fane, Novel designs for improving the performance of hollow fiber membrane distillation modules, Journal of Membrane Science, 384 (1-2) (2011) 52-62

[6] I. Noda, D. G. Brown-West and C. C. Gryte, Effect of flow maldistribution on hollow fiber dialysis-experimental studies, Journal of Membrane Science 5(1979) 209-225

[7] R. Prasad and K. K. Sirkar, Dispersion-free solvent extraction with microporous hollow-fiber modules, AIChE Journal 34 (2) (1988) 177

[8] M. J. Costello, A. G. Fane, P.A. Hogan and R. W. Schofield, The effect of shell side hydrodynamics on the performance of axial flowhollowfiber modules, Journal of Membrane Science, 80 (1993) 1-11

[9] J. Lemanski and G. G. Lipscomb, Effect of shell-side flows on hollow fiber membrane device performance, AIChE Journal 41 (1995) 2322-2326

[10]J. Wu and V. Chen, Shell-side mass transfer performance of randomly packed hollow fiber modules, Journal of Membrane Science 172 (2000) 59-74

[11]J. Zheng, Y. Xu and Z. K. Xu, Flow distribution in a randomly packed hollow fiber membrane module, Journal of Membrane Science 211 (2003) 263-269

[12]X. Yang, R. Wang, A. G. Fane, Chuyang Y.Tang and I. G. Wenten, Membrane module design and dynamic shear-induced techniques to enhance liquid separation by hollow fiber modules: a review, Sep. Purif. Technol., submitted (2010,August)

[13]Z. Ding, L. Liu and R. Ma, Study on the effect of flow maldistribution on the performance of the hollow fiber modules used in membrane distillation, Journal of Membrane Science, 215 (2003) 11-23

[14]L. Cheng, P. Wu and J. Chen, Modeling and optimization of hollow fiber DCMD module for desalination, J. Membr. Sci., (318) (2008) 154–166

[15]M. M. Teoh, S. Bonyadi and T.-S. Chung, Investigation of different hollow fiber module designs for flux enhancement in the membrane distillation process, J. Membr. Sci., 311 (1-2) (2008) 371-379

[16]R. Schneider, W. Hölz, R. Wollbeck and S. Ripperger, Membranes and modules for transmembrane distillation, Journal of Membrane Science, 39 (1) (1988) 25-42

[17]X. Yang, R. Wang, L. Shi, A. G. Fane and M. Debowski, Performance improvement of PVDF hollow fiber-based membrane distillation process, J. Membr. Sci., 369 (1-2) (2011) 437-447

[18]M. C. Porter, Handbook of Industrial Membrane Technology, William Andrew Inc, 1990

[19]I. Noda, D. G. Brown-West and C. C. Gryte, Effect of flow maldistribution on hollow fiber dialysis — experimental studies, Journal of Membrane Science, 5 (0) (1979) 209-225

[20]T. S, T. M, S. M, K. T, H. H and S. K., Nondestructive evaluation by x-ray computed tomography of dialysate flow patterns in capillary dialyzers, American Society Artifical Internal Organs Transaction, 34 (3) (1988) 794-799

[21]J. K. Park and H.N. Chang, Flow distribution in the fiber lumen side of a hollow fiber module, Am. Inst. Chem. Eng. J., 32 (1985) 1937-1947

[22]A. P. S. Yeo, A. W. K. Law and A. G. Fane, The relationship between performance of submerged hollow fibers and bubble-induced phenomena examined by particle image velocimetry, Journal of Membrane Science, 304 (1-2) (2007) 125-137

[23]H. Li, A.G. Fane, H.G.L. Coster and S. Vigneswaran, Direct observation of particle deposition on the membrane surface during crossflow microfiltration, J. Membr. Sci., 149 (1998) 83-97

[24]E. Fukushima, Nuclear magnetic resonance as a tool to study flow, Annu. Rev. Fluid Mech,. , 31 (1999) 95-123

[25]L. F. Gladden, Nuclear magnetic resonance in chemical engineering: principles and applications, Chem. Eng. Sci., 49 (1994) 3339-3408

[26]S. T.W.J, v. D. D, d. J. P.A and V. A. H, Quantification of water transport in plants with NMR imaging, Journal of Experimental Botany, 51 (2000) 1751-1759

[27]B. J. Pangrle, E. G. Walsh, S. C. Moore and D. DiBiasio, Investigation of fluid flow patterns in a hollow fiber module using magnetic resonance velocity imaging, Biotechnol. Tech., 3 (1989) 67

[28]B. J. Pangrle, E. G. Walsh, S. C. Moore and D. DiBiasio, Magnetic resonance imaging of laminar flow in porous tube and shell systems,, Chem. Eng. Sci., 47 (1992) 517-526

[29]B. E. Hammer, C. A. Heath, S. D. Mirer and G. Belfort, Quantitative flow measurements in bioreactors by nuclear magnetic resonance imaging, Biotechniques, 8 (1990) 327-330

[30]C. A. Heath, G. Belfort, B. E. Hammer, S. D. Mirer and J. M. Primbley, Magnetic resonance imaging and modelling of flow in hollow-fiber bioreactors, AIChE J., 36 (1990) 547-557

[31]S. Yao, M. Costello, A. G. Fane and J. M. Pope, Non-invasive observation of flow profiles and polarisation layers in hollow fiber membrane filtration modules using NMR micro-imaging, Journal of Membrane Science, 99 (1995) 207-216

[32] Graf von der Schulenburg, D.A., Vrouwenvelder, J.S., Creber, S.A., van Loosdrecht, M.C.M and Johns, M.L. (2008), Nuclear Magnetic Resonance Microscopy Studies of Membrane Biofouling, *J. Memb. Sci.*, **323**(1), 37-44.

[33] Creber, S.A., Vrouwenvelder, J.S., van Loosdrecht, M.C.M and Johns, M.L. (2010), Chemical cleaning of biofouling in reverse osmosis membranes evaluated using magnetic resonance imaging, *J. Memb. Sci.***362**(1-2), 202-210.

[34]S. Laukemper-Ostendorf, H. D. Lemke, P. Blümler and B. Blümich, NMR imaging of flow in hollow fiber hemodialyzers, J. Membr. Sci., 138 (1998) 287-295

[35]P. A. Hardy, C. K. Poh, Z. Liao, W. R. Clark and D. Gao, The use of magnetic resonance imaging to measure the local ultrafiltration rate in hemodialyzers, J. Membr. Sci., 204 (2002) 195-205

[36]C. K. Poh, P. A. Hardy, Z. J. Liao, Z. Huang, W. R. Clark and D. Gao, Effect of spacer yarns on the dialysate flow distribution of hemodialyzers: a magnetic resonance imaging study, ASAIO J, 49 (2003) 440-448

[37]X. Yang, R. Wang, L. Shi, A. G. Fane and M. Debowski, Performance improvement of PVDF hollow fiber-based membrane distillation process, Journal of Membrane Science, 369 (1-2) (2011) 437-447

[38]M. Sahimi, Applications of Percolation Theory, Taylor & Francis, Bristol, 1994

[39]R. C. Reid, J. M. Prausnitz and T. K. Sherwood, The Properties of Gases and Liquids, 3rd edn., McGraw-Hill, New York, 1977

List of Figures:

Fig.1. Novel module designs and fiber arrangements: (a) Randomly-packed module; (b) Semicurly-fiber module; (c) Curly-fiber module; (d) Spacer-knitted module

Fig. 2. Schematic of NMR experiments for flow inspection in membrane modules

Fig.3. Top-bottom and side-view NMR images of multi-fiber membrane modules (a) Randomly-packed module; (b) Spacer-knitted module; (c) Semicurly-fiber module; (d) Curly-fiber module(the membrane matrix appears as dark rings, the imaging slice thickness is 5 cm, 256x256 pixels)

Fig. 4. Comparison of propagator experiments for DI water in Y and Z directions of the multi-fiber membrane modules [volumetric flow rate Qf=100mL/min, slice thickness = 5 cm, DeltaΔ (observation time) =100ms]

Fig.5. Cross-sectional velocity maps of multi-fiber membrane modules (a) Randomly-packed module; (b) Spacer-knitted module; (c) Semicurly-fiber module; (d) Curly-fiber module (The brightness of the signal represents the magnitude of the flow velocity. NMR experimental parameters: 128×128 pixels, 32 average, 5 cm slice. Gradients applied G: gradient pulse interval δ = 4ms, observation time Δ = 100 ms, Qf = 100 mL/min)

Fig. 6. Effect of feed temperature on the permeation flux for various hollow fiber module configurations [3.5% NaCl solution as feed Q_f =3 L·min-1(v_f =0.33m·s-1), Q_p =0.4 L·min-1 (v_p =0.08m·s-1), T_p =298K, T_f =323K]

Fig. 7. Cross-sectional velocity maps of spacer-knitted module at varied flowrates (The brightness of the signal represents the magnitude of the flow velocity. NMR experimental parameters: 128×128 pixels, 32 average, 5 cm slice. Gradients applied G: gradient pulse interval δ = 4ms, observation time Δ = 100 ms, Q_f = 10-2500 mL/min, ~0.017-41.7mL/Sec)

Fig. 8. Normalized NMR signal magnitude as a function of flow rate for spacer-knitted module (NMR experimental parameters: 128×128 pixels, 32 average, 5 cm slice. Gradients applied G: gradient pulse interval δ = 4ms, observation time Δ = 100 ms, Q_f = 10-2500 mL/min)

Fig. 9. Comparison of propagators for DI water in Y and Z directions of spacer-knitted module at varied flow rates [volumetric flow rate Q_f=10-100mL/min, slice thickness = 5 cm, DeltaΔ (observation time) =100ms]

Fig. 10. Comparison of the velocity distribution at a flow rate of 400mL/min vs. 1500mL/min, the loss of high velocity signal due is evident. (NMR experimental parameters: 128×128 pixels, 32 average, 5 cm slice. Gradients applied G: gradient pulse interval δ = 4ms, observation time Δ = 100 ms, Qf = 10-1500 mL/min)

Fig. 11. The change in variance as function of flow rate for the spacer-knitted module in the (a) parallel-to-flow direction and (b) perpendicular-to-flow direction. (NMR experimental parameters: 128×128 pixels, 32 average, 5 cm slice. Gradients applied G: gradient pulse interval δ = 4ms, observation time Δ = 100 ms, Q_f = 10-1500 mL/min)

List of Tables

Table 1 Module specifications and membrane properties

Table 2Overall comparison for various configurations

(a) Randomly-packed module   (b) Spacer-knitted module
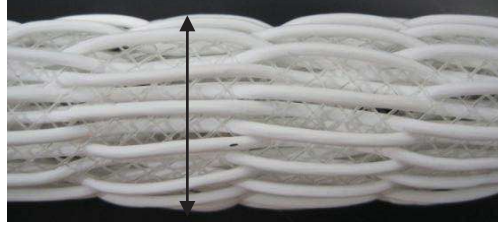
(c) Semicurly-fiber module   (d) Curly-fiber module

Fig. 1. Novel module designs and fiber arrangements: (a) Randomly-packed module; (b) Spacer-knitted module; (c) Semicurly-fiber module; (d) Curly-fiber module.
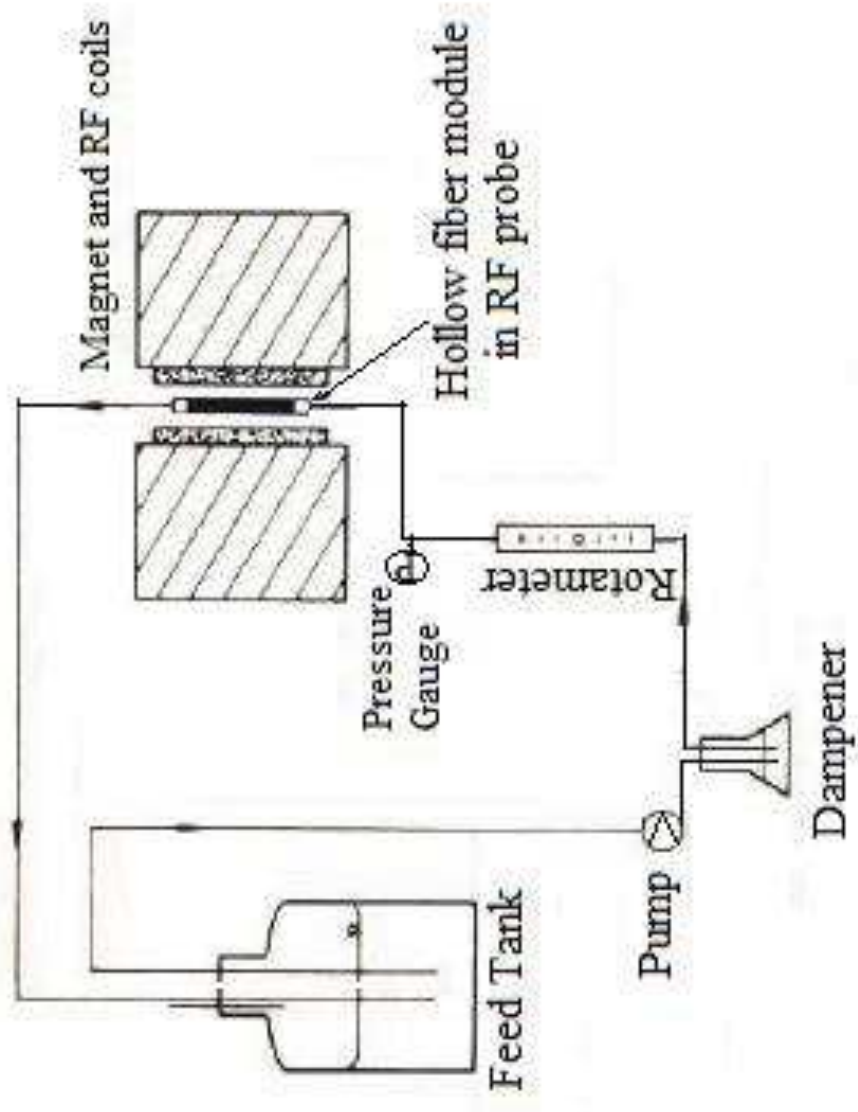
Fig. 2. Schematic of NMR experiments for flow inspection in membrane modules

Bottom-top
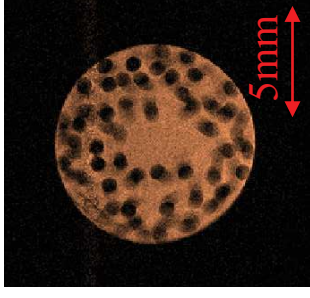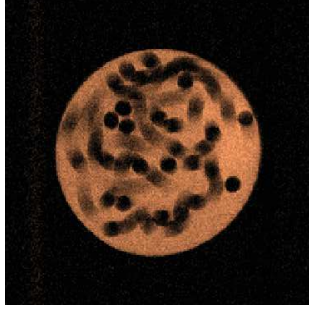
Side-view
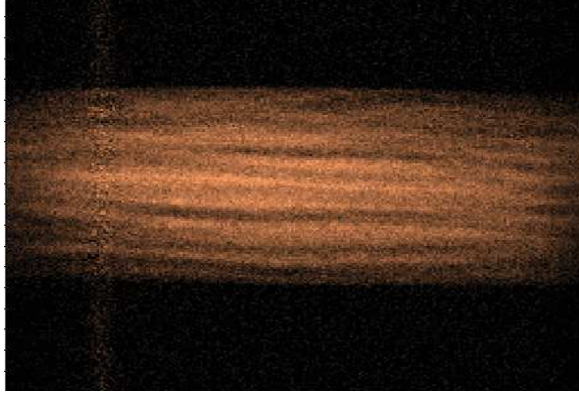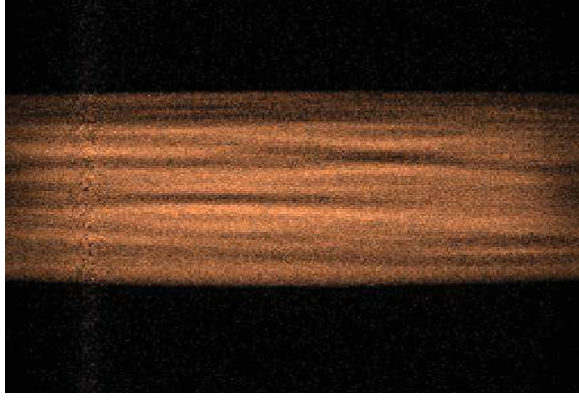
(a) Randomly-packed module   (b) Spacer-knitted module
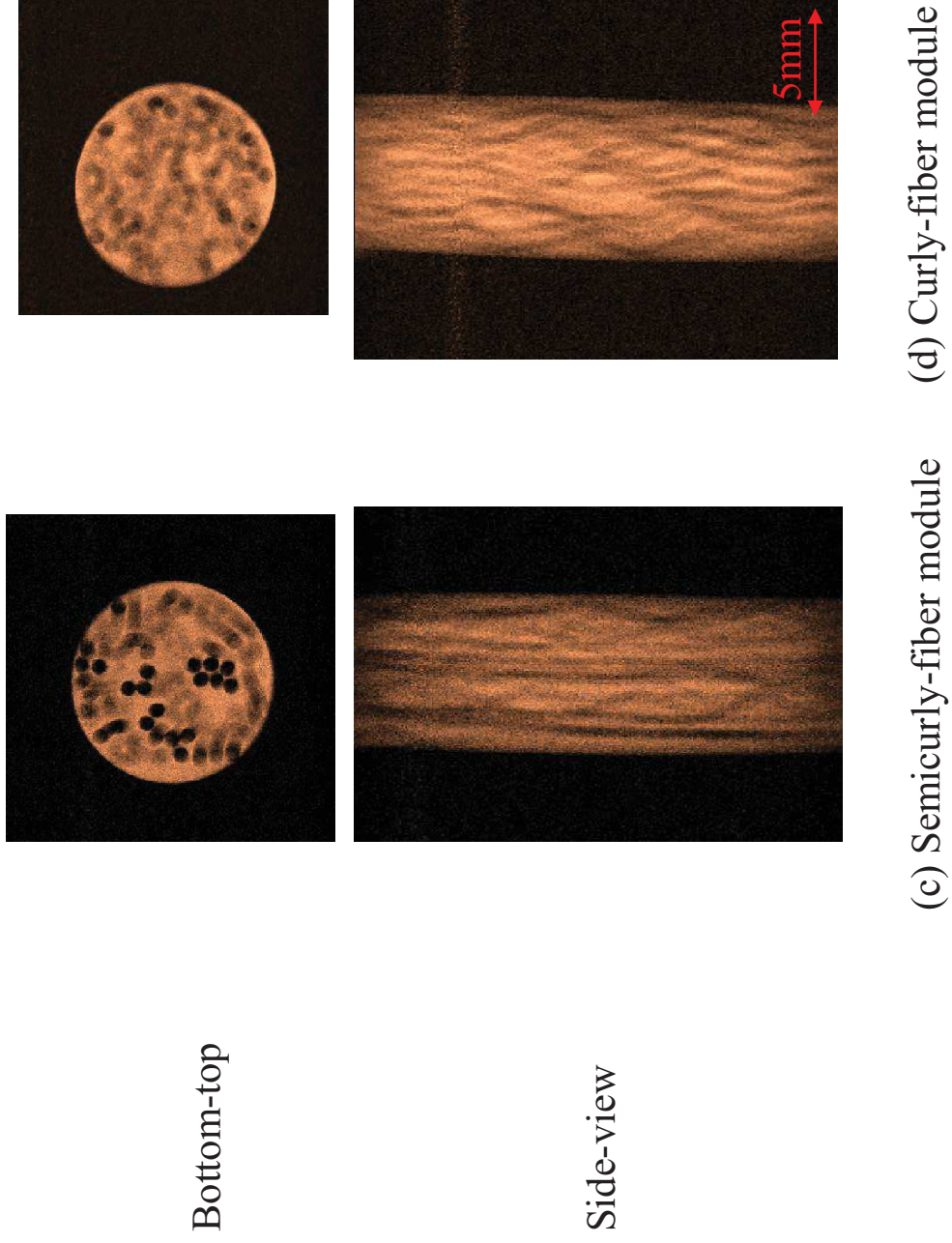
Bottom-top

Side-view

5mm

(c) Semicurly-fiber module   (d) Curly-fiber module

Fig. 3. Top-bottom and side-view NMR images of multi-fiber membrane modules
(a) Randomly-packed module; (b) Spacer-knitted module; (c) Semicurly-fiber module; (d) Curly-fiber module
(the membrane matrix appears as dark rings, the imaging slice thickness is 5 cm, 256 256 pixels)

(a) Propagators at axial Y direction
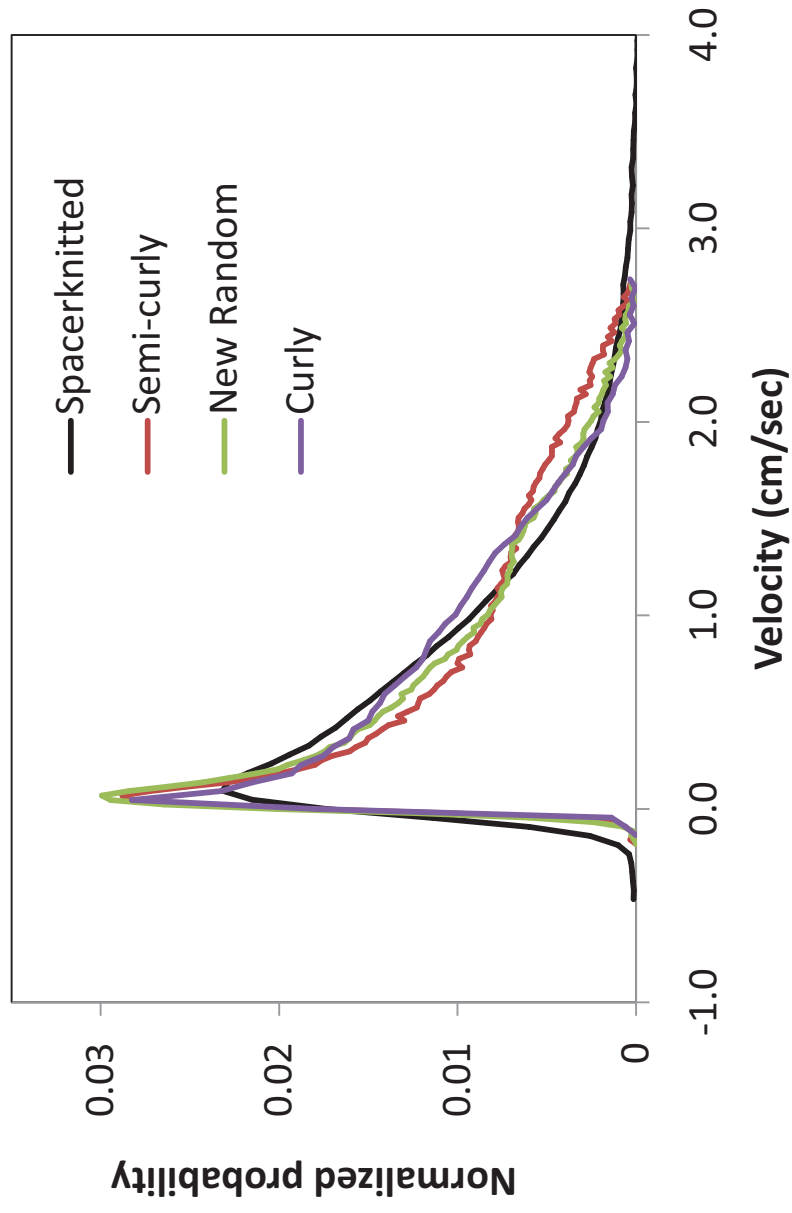
(b) Propagators at transverse Z direction

Fig. 4. Comparison of propagator experiments for DI water in Y and Z directions of the multi-fiber membrane modules [volumetric flow rate Q_f=100mL/min, slice thickness = 5 cm, Δ (observation time) =100ms]

Velocity (mm/sec)

20   15   10   5   0

(a) Randomly-packed module   (b) Spacer-knitted module

(c) Semicurly-fiber module   (d) Curly-fiber module

Fig. 5. Cross-sectional velocity maps of multi-fiber membrane modules
(a) Randomly-packed module; (b) Spacer-knitted module; (c) Semicurly-fiber module; (d) Curly-fiber module
(The brightness of the signal represents the magnitude of the flow velocity. NMR experimental parameters:
128×128 pixels, 32 average, 5 cm slice. Gradients applied G: gradient pulse interval $\delta = 4$ms,
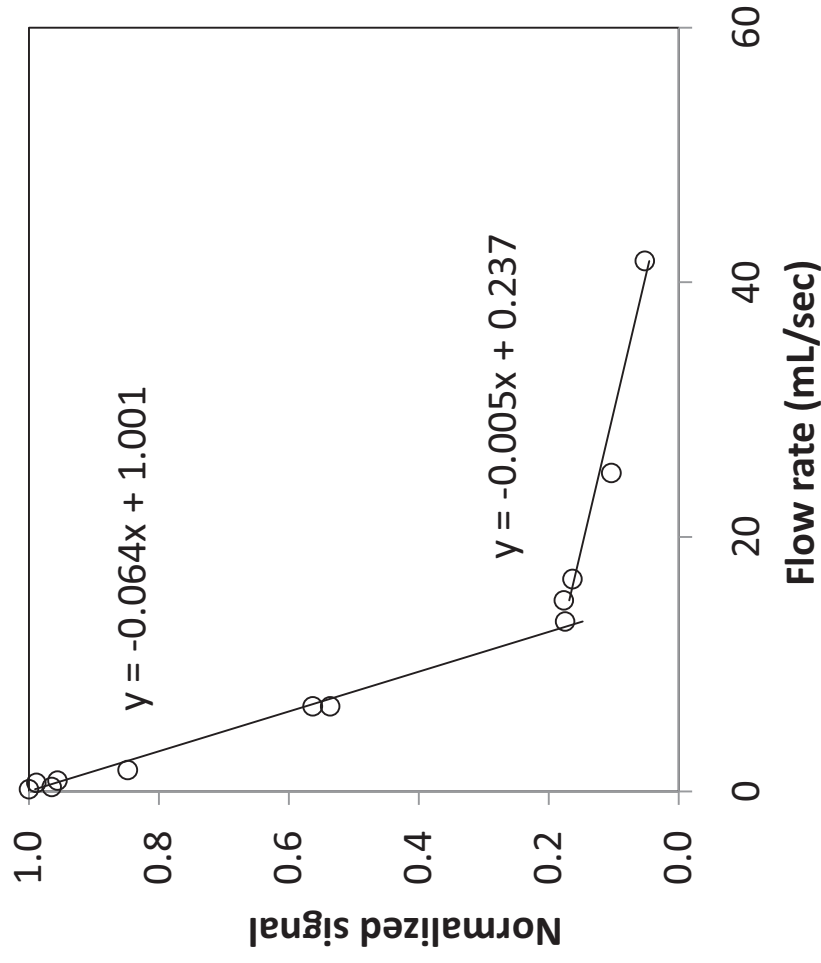observation time $\Delta = 100$ ms, $Q_f = 100$ mL/min)

Fig. 6. Effect of feed temperature on the permeation flux for various hollow fiber module configurations [3.5% NaCl solution as feed Q_f =3 L·min^{-1}(v_f =0.33m·s^{-1}), Q_p =0.4 L·min^{-1} (v_p =0.08m·s^{-1}), T_p =298K, T_f =313 − 343 K]
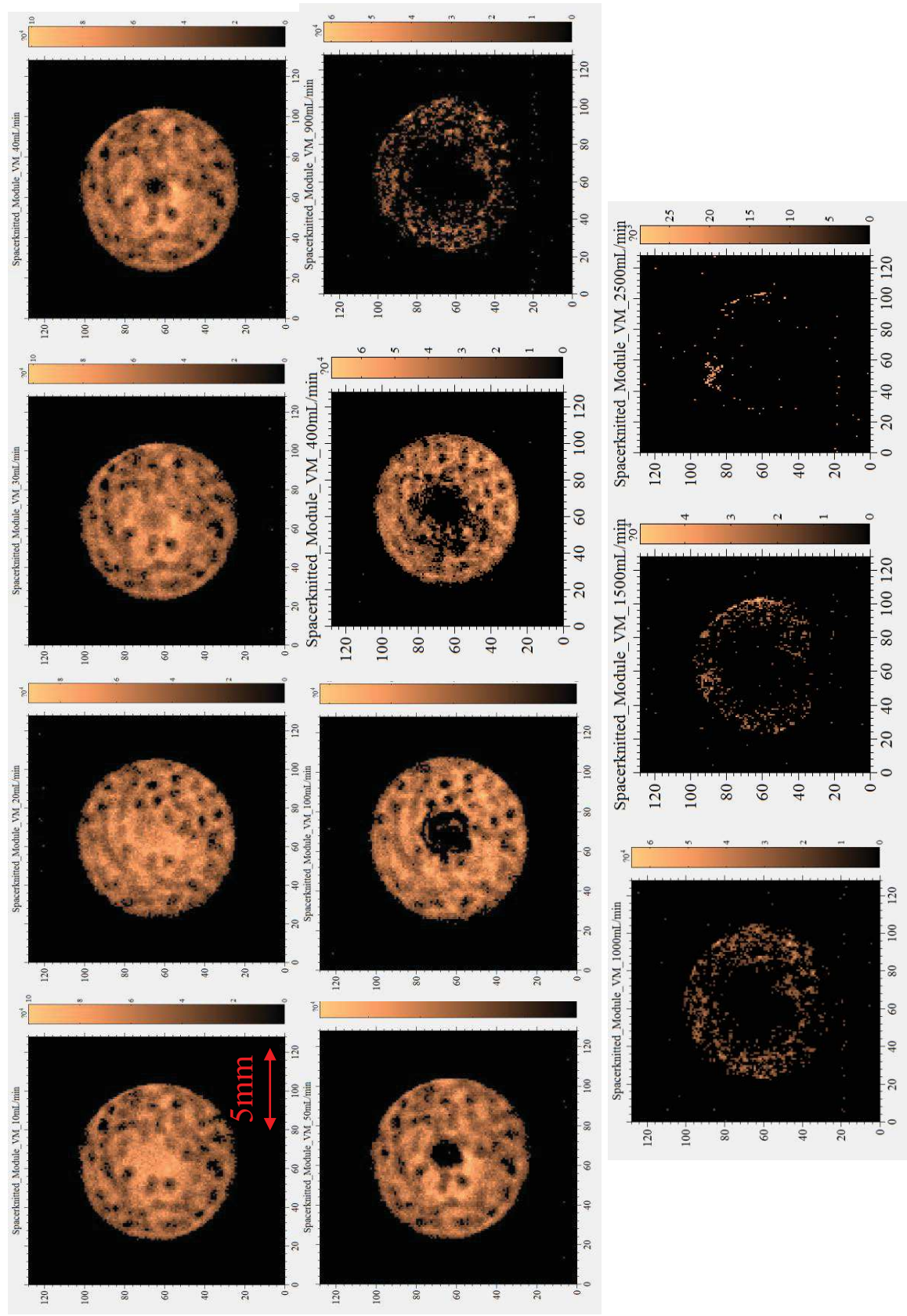
Fig. 7. Cross-sectional velocity maps of spacer-knitted module at varied flowrates (The brightness of the signal represents the magnitude of the flow velocity. NMR experimental parameters: 128×128 pixels, 32 average, 5 cm slice. Gradients applied G: gradient pulse interval $\delta = 4$ms, observation time $\Delta = 100$ ms, $Q_f = 10$-2500 mL/min, ~0.017-41.7mL/Sec)

Fig. 8. Normalized NMR signal magnitude as a function of flow rate for spacer-knitted module (NMR experimental parameters: 128×128 pixels, 32 average, 5 cm slice. Gradients applied G: gradient pulse interval δ = 4ms, observation time Δ = 100 ms, Q_f= 10-2500 mL/min)

(a) Velocity distribution at axial Y direction
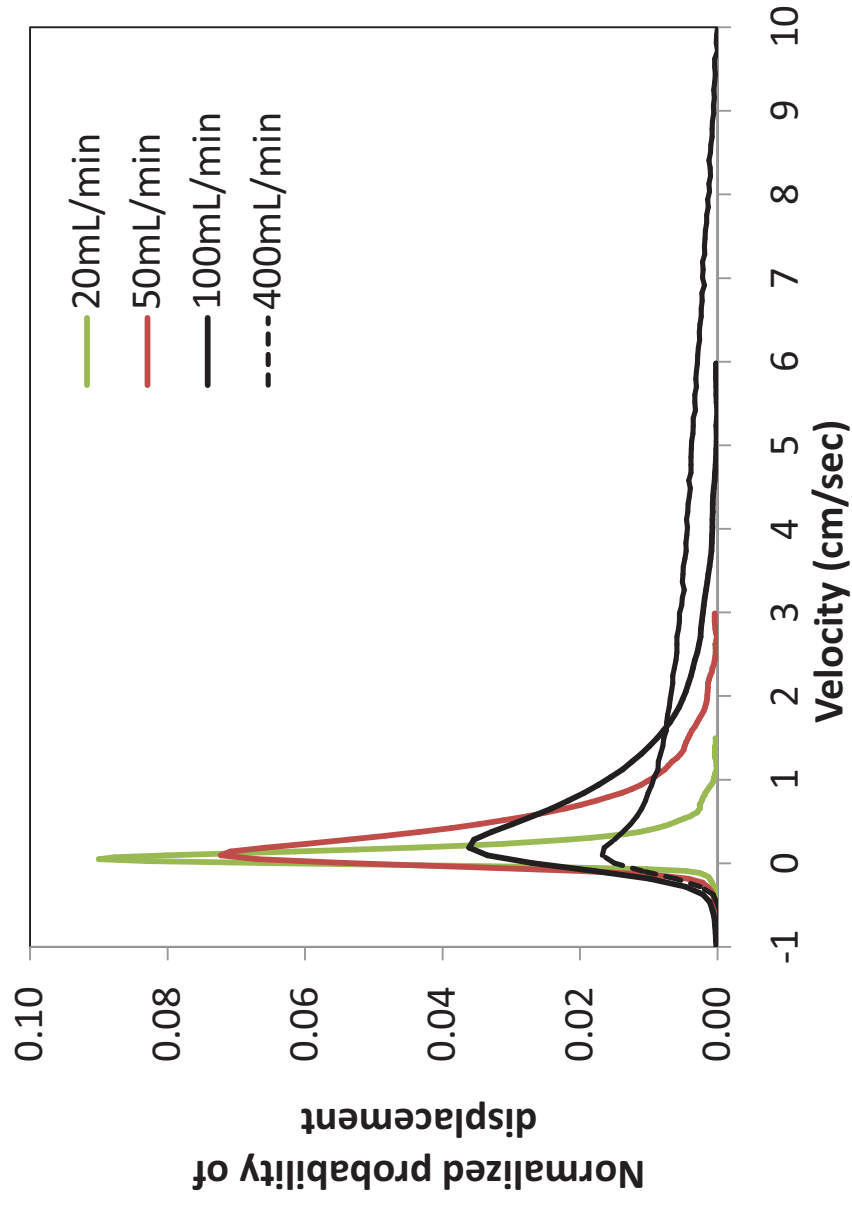
(b) Velocity distribution at transverse Z direction
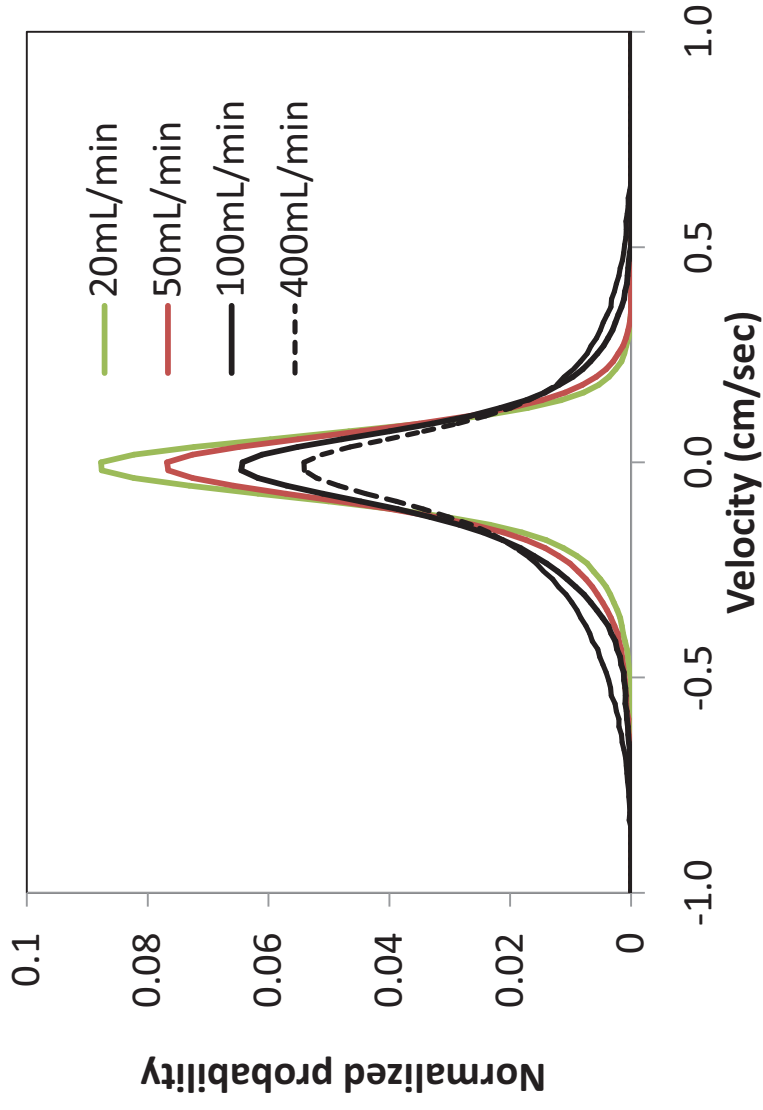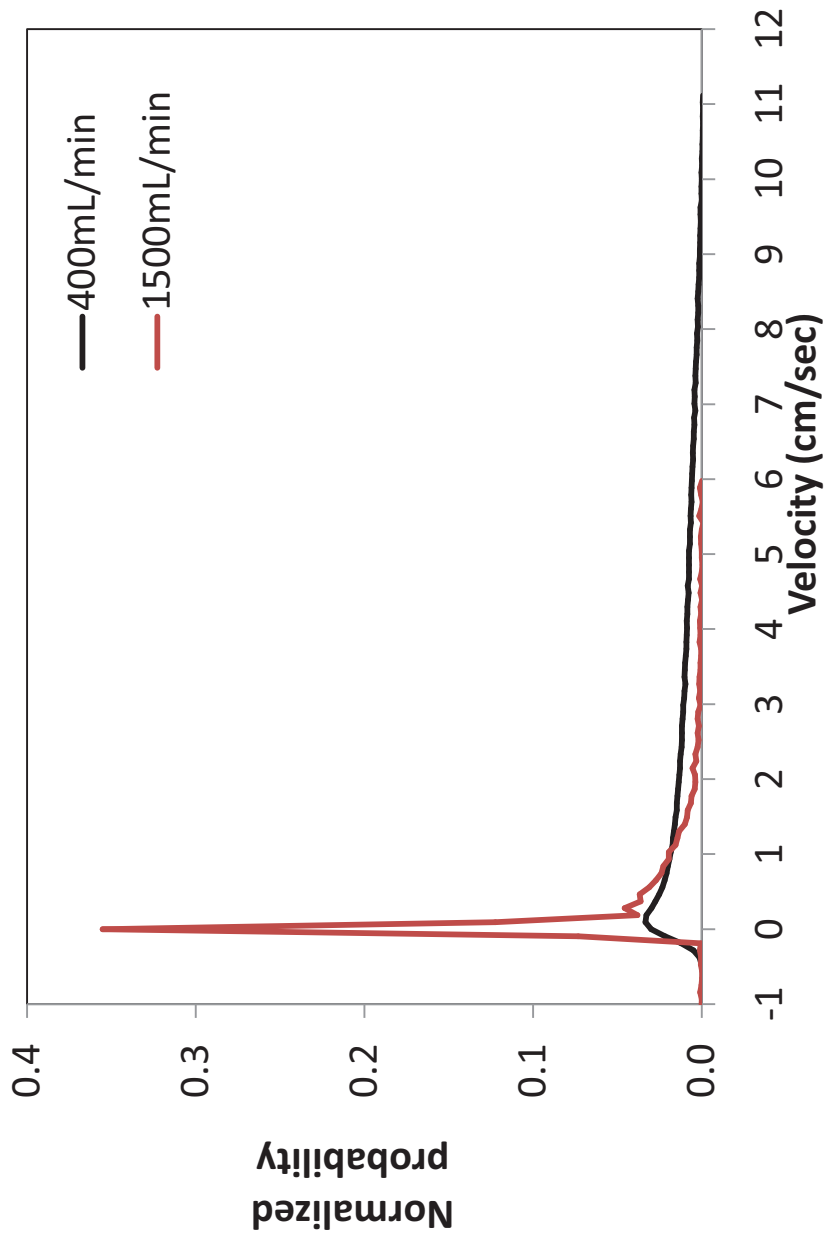
Fig. 9. Comparison of the velocity distribution for DI water in Y and Z directions of spacer-knitted module at varied flow rates [volumetric flow rate Q_f=20-400mL/min, slice thickness = 5 cm, DeltaΔ (observation time) =100ms]
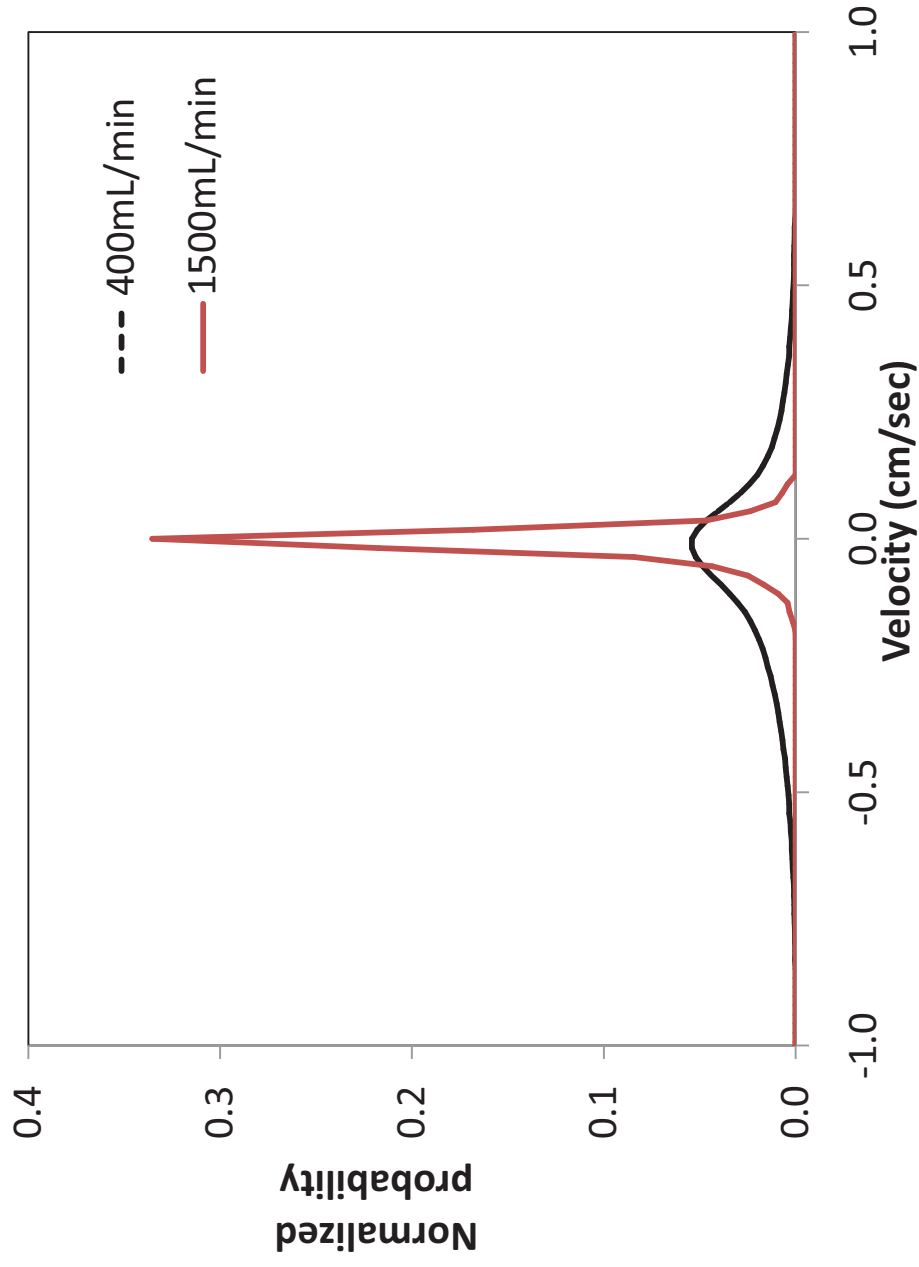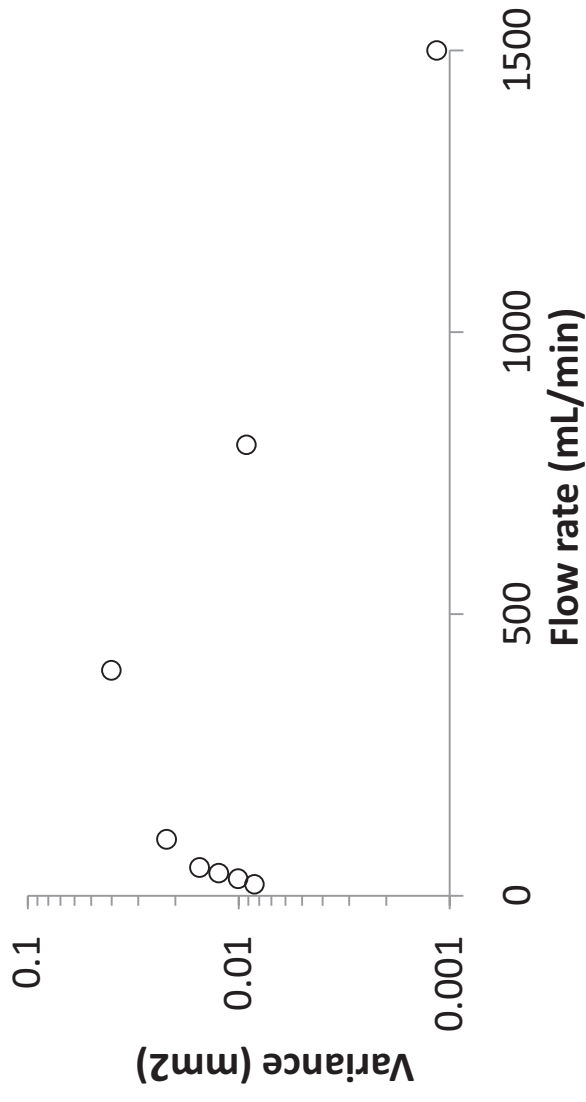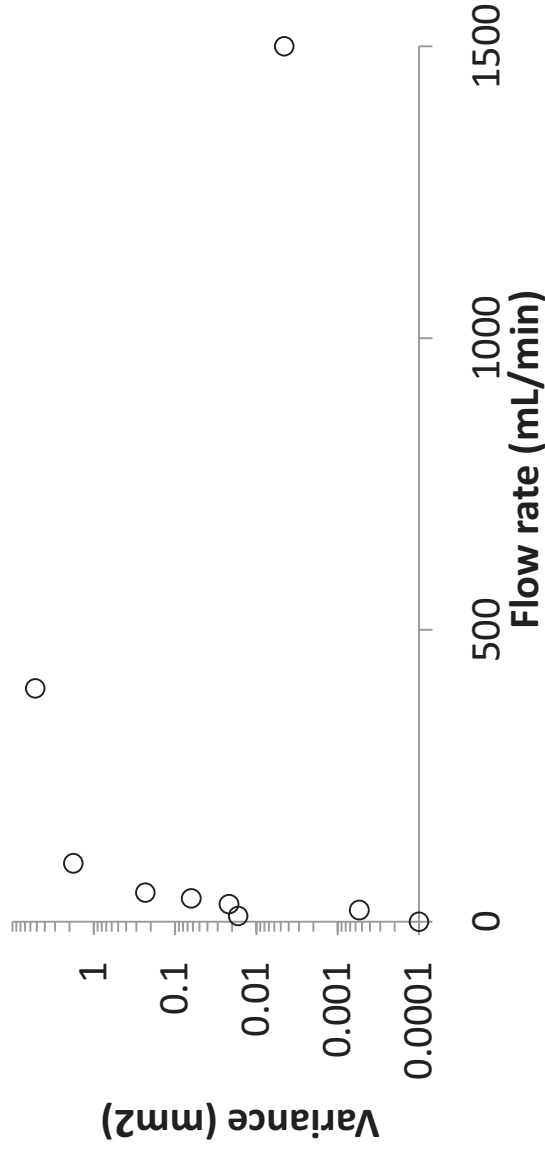
Fig. 10. Comparison of the velocity distribution at a flow rate of 400mL/min vs. 1500mL/min, the loss of high velocity signal due is evident. (NMR experimental parameters: 128×128 pixels, 32 average, 5 cm slice. Gradients applied G: gradient pulse interval $\delta = 4$ms, observation time $\Delta = 100$ ms, $Q_f = 400$-1500 mL/min)

Fig. 11. The change in variance as function of flow rate for the spacer-knitted module in the (a) parallel-to-flow direction and (b) perpendicular-to-flow direction. (NMR experimental parameters: 128×128 pixels, 32 average, 5 cm slice. Gradients applied G: gradient pulse interval $\delta = 4ms$, observation time $\Delta = 100$ ms, $Q_f = 10\text{-}1500$ mL/min)

Table 1 Module specifications and membrane properties

Module specifications

Membrane type	Housing diameter, d_s	No of fibers, n	Effective fiber length L, mm	Packing density ϕ, %	Membrane area A, m²	Remark
PVDF	19 mm	51	450	30	0.1-0.12	The winding angle is taken into account to calculate membrane area of the curly-fiber module

Membrane properties

Dimension	Pore size (μm)	Contact angle (°)	Porosity ε (%)	LEPw (Bar)	Tensile modulus E_t, MPa	Strain at break δ_b, %
d_o: 1.45 mm δ_m: 235 μm	r_{max}: 0.125 r_{mean}: 0.082	106–120	82–85	3.5	42.05	105.4

Table 2 Overall comparison for various configurations (data obtained from displacement probability distributions, Q_f=100mL/min, Δ=100ms)

Configuration	Parallel-to-flow (Y)		Perpendicular-to-flow (Z)		Skewness (mm^3)
	Mean displacement <x>, mm	Variance, σ^2, mm^2	Mean displacement <x>, mm	Variance, σ^2, mm^2	
Randomly packed module	0.70	0.36	-0.02	0.01	7.10E-02
Spacer-knitted module	0.67	0.41	-0.01	0.02	3.87E-02
Semicurly -fiber module	0.72	0.45	0.00	0.03	1.61E-02
Curly-fiber module	0.71	0.31	0.07	0.05	1.24E-02